Check for updates

Chemical trends of deep levels in van der Waals semiconductors

Penghong Ci [1,2], Xuezeng Tian [3], Jun Kang[4], Anthony Salazar[1], Kazutaka Eriguchi[1], Sorren Warkander [1], Kechao Tang[1], Jiaman Liu[1], Yabin Chen[1,5], Sefaattin Tongay[6], Wladek Walukiewicz[2], Jianwei Miao [3], Oscar Dubon[1,2] & Junqiao Wu [1,2 ✉]

Properties of semiconductors are largely defined by crystal imperfections including native defects. Van der Waals (vdW) semiconductors, a newly emerged class of materials, are no exception: defects exist even in the purest materials and strongly affect their electrical, optical, magnetic, catalytic and sensing properties. However, unlike conventional semiconductors where energy levels of defects are well documented, they are experimentally unknown in even the best studied vdW semiconductors, impeding the understanding and utilization of these materials. Here, we directly evaluate deep levels and their chemical trends in the bandgap of MoS_2, WS_2 and their alloys by transient spectroscopic study. One of the deep levels is found to follow the conduction band minimum of each host, attributed to the native sulfur vacancy. A switchable, DX center - like deep level has also been identified, whose energy lines up instead on a fixed level across different hosts, explaining a persistent photoconductivity above 400 K.

[1] Department of Materials Science and Engineering, University of California, Berkeley, CA 94720, USA. [2] Materials Sciences Division, Lawrence Berkeley National Laboratory, Berkeley, CA 94720, USA. [3] Department of Physics & Astronomy and California NanoSystems Institute, University of California, Los Angeles, CA, USA. [4] Beijing Computational Science Research Center, Beijing, China. [5] School of Aerospace Engineering, Beijing Institute of Technology, Beijing, China. [6] School for Engineering of Matter, Transport, and Energy, Arizona State University, Tempe, AZ 85287, USA. ✉email: wuj@berkeley.edu

Defects with energies falling within the bandgap may act as a trap or emitter of free charge carriers[1], a site for exciton recombination[2], and a center to scatter electrons or phonons[3]. In conventional semiconductors, native defects such as vacancies introduce levels close to the middle of the bandgap when the material is more covalently bonded, or close to the band edges when the material is more ionically bonded, resulting in the former materials being defect sensitive while the latter materials are relatively defect tolerant[4]. Comparing positions of defect levels across different host materials helps to reveal chemical trends that inform defect models with broad impact. For example, the deep level associated with a given impurity[5] or native defect[6] tends to lie universally at a fixed energy position with respect to the vacuum level even when doped in different semiconductors, which can be used to determine band alignments of the host materials; equilibrium native defects tend to drive the Fermi level toward a stabilization position, and this position with respect to the bandgap can be used as a descriptor of doping propensity and doping limit of the semiconductor[7]; the DX center, an metastable defect switchable between deep and shallow states, dominates the free electron density in III-V semiconductor alloys[8]. It is critical to ask whether such insights and knowledge attained in studying conventional semiconductors are applicable in vdW materials. New effects of defects may emerge because the layered nature of vdW materials allows stronger lattice relaxation as well as new types of defects such as intercalated atoms.

Scanning tunneling microscopy (STM) is able to experimentally visualize various types of defects on the surface and relate these imperfections to electronic structures in vdW crystals[9], in particular for the most abundant native point defects that play a critical role in their electrical[10–13], optical[2], magnetic[14], catalytic[15] and sensing properties[16]. However, STM studies have led to inconsistency on the defect types with transmission electron microscopy investigations, as well as discrepancy in signatures of defect-induced mid-gap states from theoretical calculations[1,3,17–21], largely because of unclear differentiation of STM contrast between the metal and chalcogen sublattices and the complicated convolution of electronic and geometric structures[9]. Furthermore, it shows very limited capability in detecting defects beneath the surface.

In this work, we use deep level transient spectroscopy (DLTS), a high-frequency capacitance transient thermal scanning method[22,23], to characterize electronic structures of the deep traps inside the bandgap of vdW semiconductors, particularly MoS_2, WS_2 and their alloys, including their energy positions and capture cross sections. Combined with atomic-resolution scanning transmission electron microscopy and first-principles calculations, one of the deep levels determined by DLTS is identified as sulfur vacancies, whose energy position follows the conduction band edge in the host materials, distinct from vacancy defects in traditional group III-V semiconductors. A metastable DX center is identified in these vdW semiconductors, featuring a persistent photoconductivity above 400 K and explaining the chemical trend of native electron concentration in the hosts.

Results

DLTS devices and DLTS spectra.
Mechanically exfoliated, multilayer (~ 50 nm) flakes of freshly grown $Mo_{1−x}W_xS_2$ ($x = 0, 0.4, 0.7, 1$) crystals were made into two-terminal Schottky-Ohmic devices (Fig. 1a). The Schottky contact was formed by dry-stamping freshly exfoliated flakes onto pre-deposited Pt electrodes and confirmed by the $I–V$ and $C–V$ curves shown in Fig. 1e, f, both of which show the n-type conductivity of MoS_2. This maximally protects the depletion region at the Schottky contact against contamination and damage[24], as it is at this region where

the deep levels trap and emit charge carriers during the DLTS measurement. The measured total capacitance (Supplementary Fig. 10) is composed of that of the DLTS device (C_{device}) and the stray capacitance (C_{stray}) connected in parallel. The latter, although with a large value, is insensitive to the external differential voltage (Supplementary Fig. 10), hence the variation of capacitance under the biased voltage indeed probes the former (Fig. 1f).

The depletion width at the Schottky junction (~ 20 nm, the shadow in Fig. 1d), hence the capacitance (Fig. 1c), is initially held constant by a steady-state reverse bias ($V_R = −0.5$ V, stage ①)[23]. An opposite voltage pulse (V_P) is then added onto V_R, reducing the depletion width (as evidenced by the increased capacitance at less-negative voltage, Fig. 1f), and allowing the traps in the initial depletion region to be filled with free electrons (stage ②)[23]. When the initial, constant bias is restored, the return of the capacitance to the steady-state value is characterized by a transient (stage ③) related to the emission of majority carriers from the deep traps in the material. The capacitance difference within a rate window (between the pre-set t_2 and t_1 in Fig. 1c)[22] reaches the maximum at a specific temperature. The emission rate (e_n) in stage ③ depends exponentially on temperature via the trapping energy level (E_i) measured from the conduction band minimum (CBM, E_{CB})[22],

$$\frac{e_n}{T^2} = K\sigma_n \exp\left(-\frac{|E_{CB} − E_i|}{k_B T}\right) \qquad (1)$$

where σ_n is the capture cross section, and K is a known constant. Arrhenius plots of Eq. (1) at various rate windows (0.5 ms to 20 ms in Fig. 2a) allow extraction of the activation energy of deep levels, $E_{CB}–E_i$. For MoS_2 we found two, 0.27 ± 0.03 eV (peak A) and 0.40 ± 0.02 eV (peak B), as shown in Fig. 2b. The positively valued DLTS peaks (Fig. 2a) indicates that these are majority carriers traps in MoS_2[22]. We also measured current transient spectroscopy (CTS, see Supplementary Fig. 1) by recording the current rather than capacitance under the pulsed bias[25], yielding an activation energy of $E_{CB}–E_i = 0.25 \pm 0.02$ eV for MoS_2 (Supplementary Fig. 1a), consistent with the peak A in DLTS. We note that for each of the trap energies obtained in this work, at least two devices were measured and all show consistently very similar energy. Thermodynamically, the slope of Eq. (1) corresponds to the change of enthalpy (ΔH), different from the Gibbs free energy ΔG (= $E_{CB}–E_i$)[26], but the difference can be neglected when electrons are excited from the traps to the conduction band without invoking changes in the bonding configuration (see Supplementary Note 5)[27].

Determination of sulfur vacancies from STEM and DFT calculations.
To reveal the atomic origin of these deep traps, we have performed first-principles calculations of S single vacancies (V_S) in multilayer MoS_2, WS_2 and their alloys. V_S is chosen because it is the most abundant defect known to naturally occur in these materials[21]. The calculation shows that V_S would introduce a deep-level state with energy of 0.29 eV (for MoS_2) and 0.21 eV (for WS_2) below the CBM, in good agreement with the DLTS/CTS results. We note that the value of 0.29 eV is also consistent with the calculated V_S energy in MoS_2 previously reported in literature[1,3]. Our calculations also confirm that V_S is a deep acceptor, labeled as $(0/−)$[1,23], not responsible for the natively n-type conductivity of MoS_2. The neutral ground state implies its extremely weak Coulomb attraction to electrons, and hence very small capture cross section. V_S defects are directly observed in these materials by scanning transmission electron microscopy (STEM, Fig. 1b and Supplementary Fig. 5)[11], where the density of V_S is directly determined to be $1\sim3 \times 10^{20}$ cm$^{−3}$
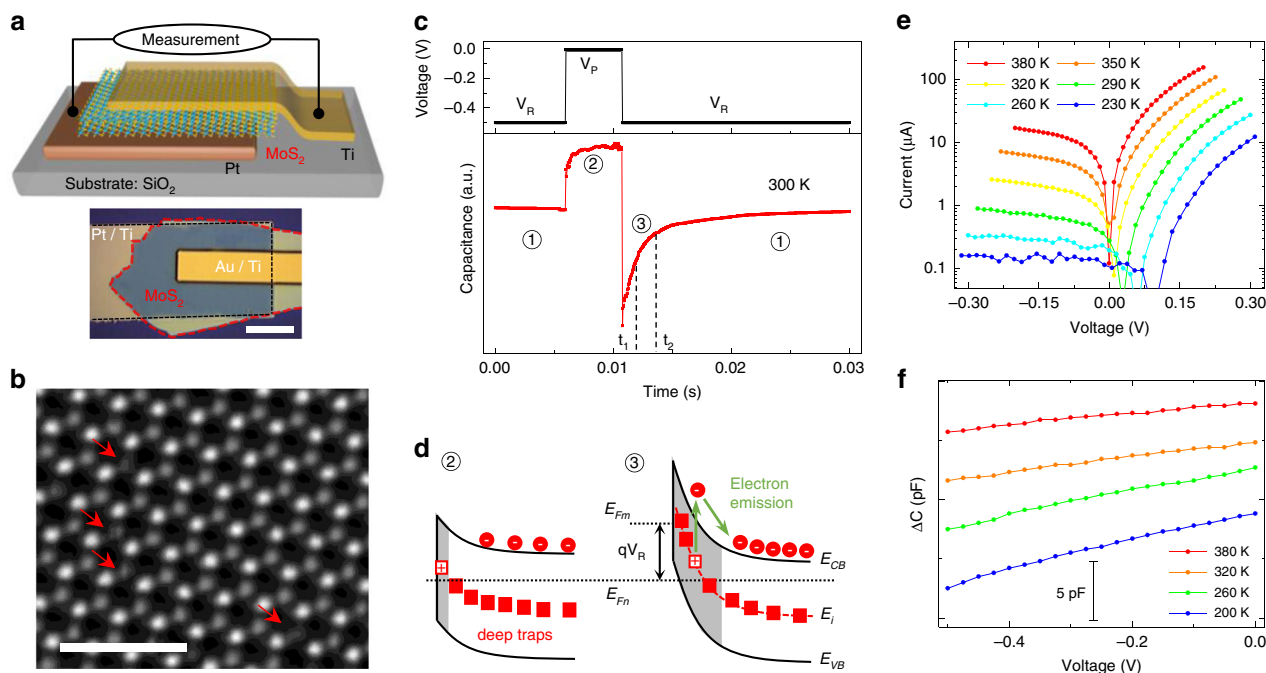
Fig. 1 Materials and devices for transient spectroscopic study of defects. a Schematic and optical image (scale bar: 20 μm) of an asymmetric MoS_2 device for DLTS, with Schottky contact (MoS_2/Pt/Ti) on the bottom and Ohmic contact (Au/Ti/MoS_2) on the top. **b** Aberration-corrected STEM image of a monolayer MoS_2 exfoliated from the materials used for devices. Red arrows highlight S vacancies (V_S). Scale bar, 1 nm. **c** Capacitance transient (bottom) in response to a pulsed change in bias voltage (top). **d** Band bending of the Schottky junction (MoS_2/Pt), illustrating the electron trapping (②) and emission process (③) of deep traps in the depletion region (shaded). V_R tunes the Fermi level of the n-type MoS_2 (E_{Fn}) with respect to that of the metal contact (E_{Fm}). **e** & **f**, Temperature-dependent I–V and C–V curves confirming the Schottky-Ohmic contacts.
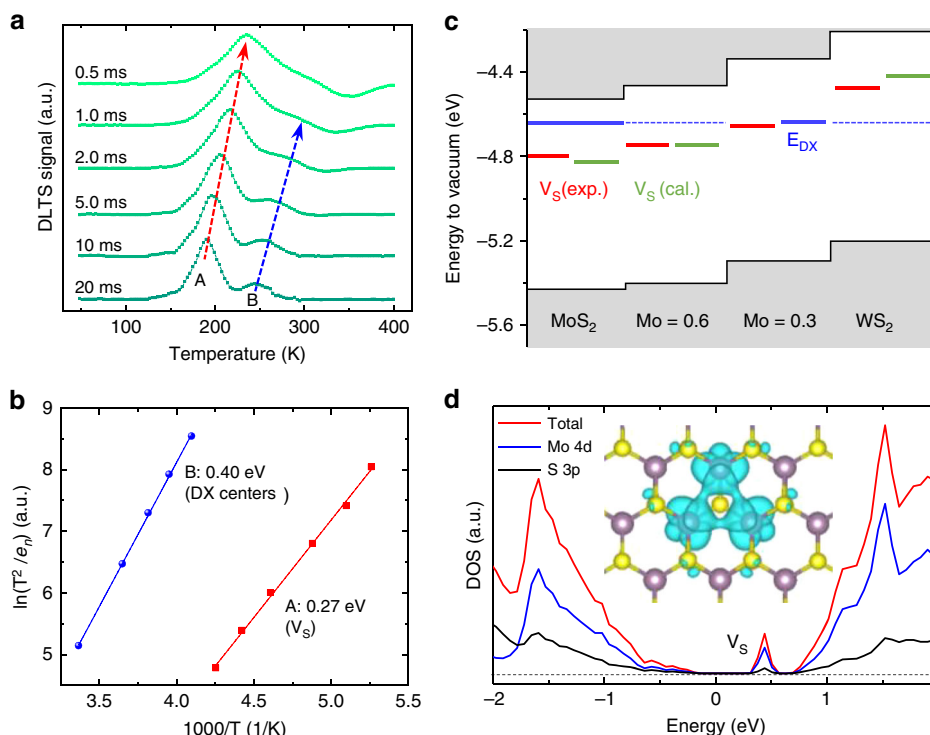
Fig. 2 Deep levels and their alignment in vdW crystals. a DLTS signal of a MoS_2 device at different rate windows and **b** the resultant Arrhenius plots to determine the activation energies. **c** Conduction and valence band edge alignment calculated with respect to the vacuum level, and positions of deep level experimentally identified in this work. Solid black lines: CBM and VBM in bulk crystals from our DFT calculations; red bars: deep levels attributed to V_S measured by DLTS and CTS; blue bars: DX center levels determined by DLTS and PPC (dashed blue line is guide to the eye); green bars: DFT-calculated V_S levels. **d** density of states (DOS) for multilayer MoS_2 with V_S. Inset: real space distribution of the wavefunction of V_S state. The purple and yellow spheres represent Mo and S atoms, respectively.

(Supplementary Fig. 4), on the same order of those reported in literature[3,21]. The STEM study also confirms that V_S is the dominant point defects, and no other defects or impurities were detected in the materials. We note that akin to conventional semiconductors, not all of these V_S are electronically active (Supplementary Fig. 6); in fact, deep traps can be highly passivated or compensated, as observed in GaN and GaAs[28,29].

To reveal the chemical trend of the V_S level in different vdW semiconductors, $Mo_{0.6}W_{0.4}S_2$, $Mo_{0.3}W_{0.7}S_2$, and WS_2 were also synthesized and then assembled into Schottky devices for similar DLTS/CTS measurements (Supplementary Fig. 1). All of these materials exhibit at least one deep level, akin to the feature A observed in MoS_2, with an energy level below the CBM of the host material of 0.29 ± 0.02 eV, 0.31 ± 0.02 eV and 0.26 ± 0.04 eV (red bars in Fig. 2c), respectively. These energy levels are all in good agreement with the DFT calculated V_S levels, as shown by the green bars in Fig. 2c and the refined band structure with V_S in Supplementary Fig. 8.

Some deep levels in different isovalent materials line up at a fixed position with respect to the vacuum level, such as oxygen dopant or Ga dangling bond in different $GaAs_{1-x}P_x$ alloys[6,30]. In contrast, the red bars in Fig. 2c show that as the W fraction increases in $Mo_{1-x}W_xS_2$, the energy level of V_S shifts monotonically toward the vacuum level; that is, the V_S level largely follows the CBM of the host. This is understandable because, as shown in the partial density of states plot in Fig. 2d, the V_S state originates mostly from the 4d (5d) orbitals of the Mo (W) atoms, rather than the S atoms, sharing the same orbital composition as the CBM[31,32]. Following this finding, anion impurities (such as oxygen) substituting S are predicted to create deep levels also about 0.3 eV below the CBM of the host (see Supplementary Fig. 7), because it is known that highly electronegative, substitutional dopants tend to have similar wavefunctions as those of ideal vacancies[6]. The electron capture cross section (σ_n) of V_S is evaluated from Eq. (1) to be $\sim3.6 \times 10^{-18}$ cm^2 in MoS_2, using the thermal velocity effective mass (0.57 m_o) and effective density of states mass (0.50 m_o) obtained from our DFT calculation and literature (see Supplementary Note 1). This value is small but comparable to that of Zn acceptor level in Si and Cu acceptor level in Ge[23,33].

Persistent photoconductivity and DX center model. To explore the origin of peak B (0.40 eV) in MoS_2 shown in Fig. 2a, we obtained complementary information about deep levels from photoconductivity measurements. Photoconductivity, especially when it is persistent (persistent photoconductivity, PPC), has been used to gauge conduction by charge carriers photo-liberated from certain deep traps[34,35]. Figure 3a shows temperature-dependent dark conductance of a MoS_2 flake (~50 nm thick) measured in four-probe geometry (Inset of Fig. 3b). The sample was cooled in darkness from 400 K to 200 K (black data points). It was then exposed to white light for 10 min (blue data point) at 200 K, during which the conductance became two orders of magnitude higher than in the dark. When the light was switched off (dark again) at this low temperature, the conductance dropped slightly, but still stayed >50 times higher than the pristine dark state. The PPC stayed at this level for at least 11 h at 200 K (Fig. 3b). When the sample was warmed up, the conductance stayed at the higher level (red data points) until a temperature of 400 K where it nearly converged to the pristine dark conductance.

Such a PPC effect in response to light exposure and temperature is a direct manifestation of metastability of defect states, and a hallmark of DX centers in semiconductors[34,35]. DX centers, observed in the 1980s in many III-V semiconductors such as AlGaAs, are a special type of localized states resonant
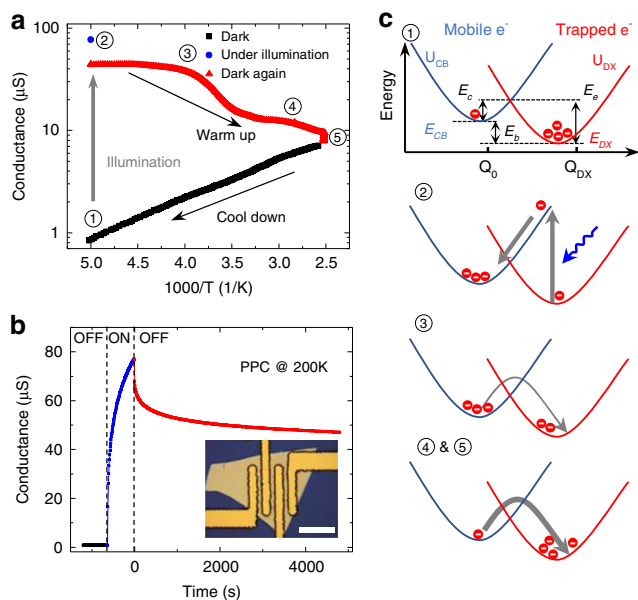

Fig. 3 Temperature-dependent persistent photoconductivity (PPC) and the DX center model. a Conductance of a MoS_2 device as a function of temperature before, during, and after exposure to light illumination. **b** PPC transient of the device at 200 K. Inset: optical image of a four-probe device for PPC measurement (scale bar: 20 μm). **c** Configurational coordinate diagram (CCD) showing the three energies to characterize the DX center and describe the five PPC processes in **a**.

with the conduction band of the host[8]. In contrast to ordinary deep levels, DX centers are capable of switching into a charge-delocalized, electron-donating state via significant lattice relaxation when triggered by external stimuli, such as light and gate control[8,36,37]. Typically described in the configurational coordinate diagram (CCD) as shown in Fig. 3c, DX centers are characterized by a parabolic coordinate (Q) dependence of DX center energy (U_{DX}) intersecting that of the delocalized state (U_{CB})[8]. The displacement along the Q axis between the two minima describes a large lattice relaxation that reflects the metastability of the DX centers. Three energies are thus defined: capture activation energy (E_c), which is the energy barrier for the DX center to trap an electron and can be determined from the kinetics of PPC; emission activation energy (E_e), the energy barrier to de-trap (emit) an electron, measured via DLTS[8,36]; and energy depth ($E_b = E_{CB}-E_{DX} = E_e-E_c$), which is the ground state energy (E_{DX}) measured from the CBM (E_{CB}) and can be derived from the temperature dependence of conductance.

As shown in Fig. 3a, c, at the thermal equilibrium state (stage ①), most electrons are trapped in the DX centers. Upon excitation by light with energies above the optical threshold (stage ②)[8,36], electrons in E_{DX} are photo-excited to E_{CB}. When the light is off, these electrons stay in E_{CB} and are blocked by the barrier E_c from relaxing back to E_{DX}, causing the PPC (stage ③). When temperature rises, more electrons are thermally excited over E_c into E_{DX} (stage ④), eventually recovering to the pristine, dark-state conductivity (stage ⑤). In this study, the PPC effect exists at temperatures up to more than 400 K (upper limit of our equipment). This is in stark contrast to the PPC effect of DX centers discovered in group III-V semiconductors, where it survives only at $T < \sim 140$ K[35,37,38].

The transient PPC curves are plotted in Fig. 4a for a range of temperatures, where non-persistent photocurrent was excluded, dark current was subtracted and the remaining part was normalized by the value at $t = 0$, the moment the illumination
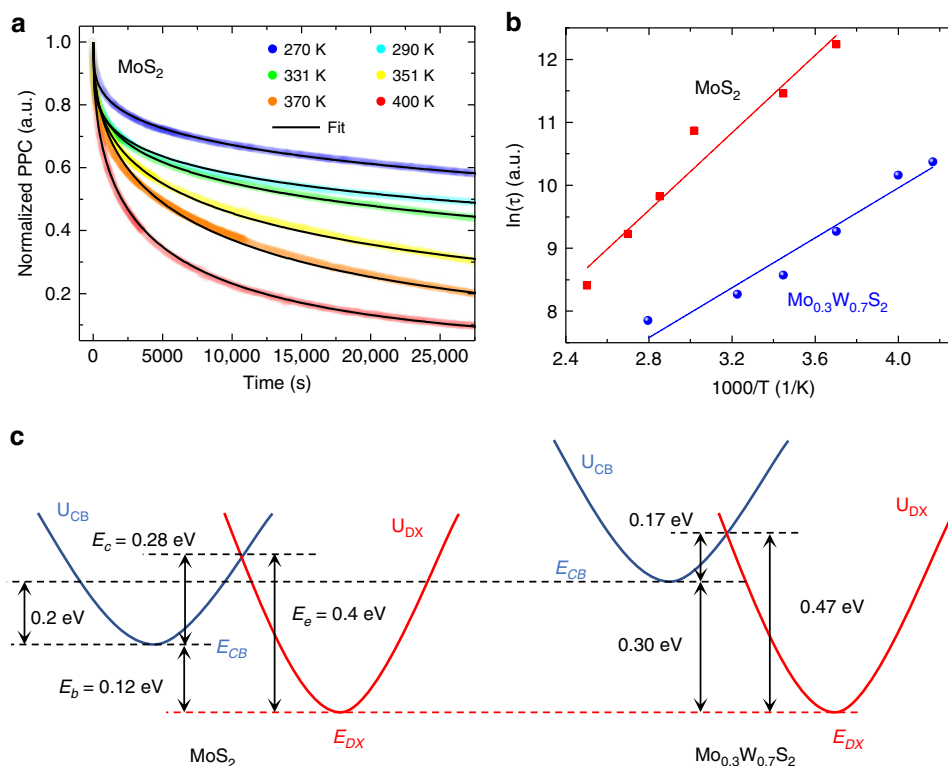
Fig. 4 DX center levels measured in MoS₂ and Mo₀.₃W₀.₇S₂. **a** Transient normalized-PPC curves at various temperatures for MoS₂ and **b** the resultant Arrhenius plots of the time constant for MoS₂ and Mo₀.₃W₀.₇S₂. Semitransparent points: experimental data; thin solid lines: fitting to Eq. (2). **c** CCD for MoS₂ and Mo₀.₃W₀.₇S₂, where the energy depth (E_b), capture (E_c) and emission (E_e) energy barriers are determined by temperature dependence of conductance, PPC and DLTS, respectively. The band offset between the two materials is obtained from DFT, resulting in a flat lineup of the DX center energy level (E_{DX}) across different host materials. The error range for these energies is estimated to be ± 0.04 eV.

is terminated. Note that in order to reset the initial dark current before taking each of these PPC curves, the samples were kept at 400 K for at least one day in a high vacuum (~10^{-6} torr) to drain the extra electrons in E_{CB}. We see that, consistent with the DX center model (Fig. 3), high temperature expedites the kinetics of the PPC decay. Following the treatment in literature, the PPC can be well described by the stretched-exponential equation[34,35]:

$$I_{PPC}(t)/I_{PPC}(0) = \exp[-(t/\tau)^\beta] \quad (2)$$

where τ is the characteristic decay time constant, β is a decay index with a value between 0 and 1. Because of the underlying thermal activation process, the temperature dependence of τ is related to the trap barrier via $\tau \propto \exp(E_c/k_B T)$[34,35]. Arrhenius plots of the temperature-dependent τ yield E_c of 0.28 ± 0.02 eV for MoS₂ and 0.17 ± 0.02 eV for Mo₀.₃W₀.₇S₂ (Fig. 4b and Supplementary Fig. 3). These values are higher than E_c (~0.14 eV) of DX centers reported in the Se-doped AlGaAs system[8], presumably because the layered structure of the vdW materials allows larger lattice relaxation than the tetrahedral structure of AlGaAs. The higher E_c is also responsible for the extension of PPC to much higher temperatures.

The energy E_b (= E_{CB}−E_{DX}) characterizes the thermodynamic energy depth of the DX center, and was extracted from Arrhenius plots of the dark conductance of the sample (Supplementary Fig. 3). Values of $E_b = 0.12$ eV and 0.30 eV were found for MoS₂ and Mo₀.₃W₀.₇S₂, respectively. Adding E_b to E_c gives E_e, the emission barrier, of 0.39 eV and 0.47 eV for MoS₂ and Mo₀.₃W₀.₇S₂, respectively. These values are in very good agreement with the energies of peak B measured in DLTS for MoS₂ (0.40 ± 0.02 eV) and Mo₀.₃W₀.₇S₂ (0.47 ± 0.02 eV). Therefore, we attribute the peak B measured in DLTS to emission of

electrons from the DX centers. We note that, unlike regular deep levels (such as the V_S state) which have no capture/emission barriers, for DX centers, the Arrhenius plot of the DLTS spectrum extracts the emission barrier E_e (Figs. 2c and 3c), rather than E_b which is the separation of E_{DX} directly measured from the conduction or valence band edges (see more in Supplementary Note 6)[23]. Following the CBM offset of ~0.3 eV between MoS₂ and WS₂ from our DFT calculation, the CBM (E_{CB}) of Mo₀.₃W₀.₇S₂ is interpolated to be higher than that of MoS₂ by 0.2 eV. Combining all these energy values, the energy of E_{DX} shows an interestingly flat alignment across these two compositions, as plotted in the CCD in Fig. 4c. It is not surprising to see that the E_{DX} position is independent of the material composition because it is also constant for DX centers in AlGaAs across different alloy compositions[8,36,38]: in AlGaAs alloys, E_{DX} is located universally at 3.8 eV below the vacuum level, and does not follow the CBM of the host material (in contrast to shallow defect levels). DX centers act as deep traps that result in different shallow donor doping efficiency in AlGaAs with different compositions[8]; similarly, the chemical trend of energy level of DX centers in the vdW semiconductors can explain the well-known, orders of magnitude higher native free electron density in undoped MoS₂ than in WS₂, as the DX centers are shallower in the former (details in Supplementary Fig. 9). When they are doped, these deep defects also largely determine the doping efficiency and dopability of these materials, as they can compensate the shallow dopants.

Discussion

Although our multipronged experiments show clear evidence of DX centers in these vdW semiconductors, elucidation of the
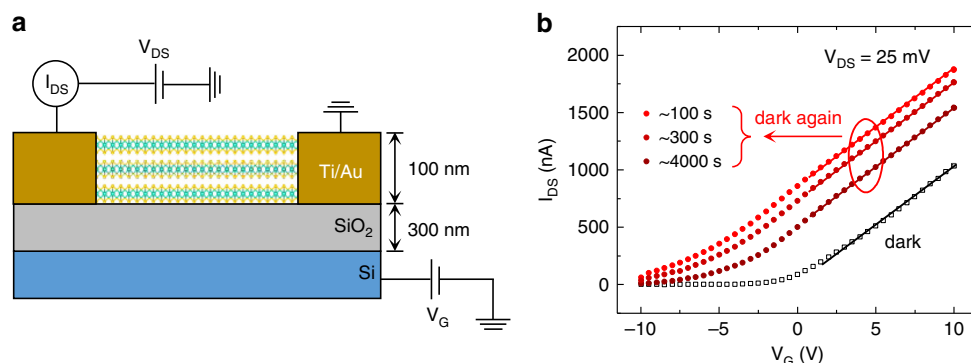
Fig. 5 Mobility of MoS$_2$ before and after illumination. a Schematic of a multilayer MoS$_2$ field-effect transistor (FET). **b** Transient transfer characteristics for the FET before the illumination (hollow points) and at specific time after the illumination is turned off (solid points). The back gate voltage, V_G, is applied to the substrate. The solid lines show the slopes of the I_{DS}–V_G curves, corresponding to electron mobility of the channel material in the device.

atomic origin of the DX centers requires further exploration including extensive first-principles calculations. However, the flat alignment of E_{DX} provides a clue. In AlGaAs, the electron wavefunction of the DX center is extremely localized on an Al/Ga site surrounded only by and bonded only to the nearest As atoms; therefore, E_{DX} is very insensitive to the change of Al fraction in the alloy[37,39]. Similarly, in Mo$_{1-x}$W$_x$S$_2$ alloys where E_{DX} is independent of the cation composition x, it is likely that the DX centers neighbor only S atoms, hence are either impurity atoms substituting the cation, or small interstitial atoms bonded to S. For example, a potential candidate would be a defect complex involving hydrogen bonded to S, a dopant inevitably and unintentionally introduced during the growth. Indeed, hydrogen has been proposed to be a possible origin of n-type native conductivity in MoS$_2$ due to the formation of shallow levels[40].

The decay time constant describes the time it takes for the mobile electrons to be re-trapped by the DX centers, and dictates the relaxation kinetics of the free charge carrier density. The transient conductivity or current in the PPC (Fig. 4a) is assumed to have a similar relaxation kinetics as that of free carrier density, and hence can be used to extract the delay time constant for DX centers. This assumption is typically made in investigation of DX centers in traditional III–V semiconductors as the carrier mobility varies much less than the carrier density and the current is then directly proportional to carrier density[34–36,41,42]. In order to test the validity of this assumption in our case, a multilayer MoS$_2$ FET was made to determine the evolution of mobility before and after the illumination. Figure 5a depicts a multilayer MoS$_2$ assembled into the FET which is subjected to a back gate voltage (V_G). According to the data in Fig. 5b, we extract the low-field field-effect mobility to be ~16 cm^2/(V S) for the MoS$_2$ channel, based on the expression $\mu = [dI_{DS}/dV_{Gate}] \times [L/WCV_{DS}]$[43], where W and L are the width and length of the channel, respectively, C is the capacitance of the gate dielectric SiO$_2$ layer, and V_{DS} is the source-drain voltage in the FET. These I_{DS}–V_G curves exhibit the same slope before and after light illumination, indicating a constant mobility regardless of the density of free or trapped electrons in the channel, hence validating the extraction of time constant from electrical current via Eq. (2).

It is technically challenging to apply the DLTS to monolayers of vdW semiconductors, owing to expected high leakage current and issues arising from the sub-depletion width thickness. However, the deep levels we quantified for thick layers are expected to be applicable to monolayers and few layers. This is because the very weak interlayer vdW coupling only modulates the conduction and valence band edges, transitioning the material from direct bandgap in monolayers to indirect bandgap in the

bulk, while hardly affecting the entire band structure[32]; on the other hand, the spatially very localized wavefunctions of deep levels do not hybridize with the conduction or valence band edges, which is in contrast to shallow defects whose wavefunctions are composed of entirely the band edge states. For example, regarding monolayer MoS$_2$, first-principles calculations predicted that the V$_S$ deep level lies about 0.5 eV below the CBM at the K point in the Brillouin Zone[1,3,17,21,44], which is in good agreement with the 0.27 eV below the CBM at the Q point in multilayer MoS$_2$ quantified in this study, considering the 0.2 eV CBM offset between monolayer and bulk MoS$_2$[45,46].

Our work determines energy levels and chemical trends of the most abundant native defects in MoS$_2$, WS$_2$ and their alloys. These energy levels offer quantitative references for both applications that are limited by defects such as transistors[10,24] and light emitting devices[2], as well as applications that are facilitated by defects such as catalysis[15] and sensors[16]. We also discover metastable and switchable, DX center-like defects in these vdW materials at temperatures above 400 K, in contrast to those in other semiconductors that exist only at $T < 140$ K[8,38]. As a result, practical device applications may be developed from the DX centers in vdW materials, such as nonvolatile memory based on a single defect. These defects may provide a platform for study of electron-phonon coupling, electron correlation, and many-body physics such as negative-U effects in quasi-two-dimensional crystals[30].

Methods

Electrical measurements. A deep level transient spectrometer (Sula Technologies) was used to measure DLTS, CTS, CV, and IV curves in Figs. 1 and 2. In this instrument, the emission rate is set as $e_n = 1/(D \times \Delta t)$, where $\Delta t = t_2 - t_1$ is the preset time difference in Figs. 1c and 2a, and D is a constant representing the delay factor, 1.94 and 4.3 for the DLTS and CTS measurements, respectively. In the capacitance test, including CV and DLTS, an A.C. voltage with an amplitude of ~60 mV and frequency of 1 MHz was superimposed onto the D.C. reverse bias. For the PPC measurements, four-terminal transport characteristics were measured by applying a DC bias to the outer channel and recording the current using a current amplifier and the voltage drop across the inner channel using a voltage amplifier. Optical illumination for the PPC was by a convection-cooled 30-Watt illuminator (Fiber-Lite 190).

STEM characterization. Mechanically-exfoliated monolayer MoS_2 was transferred from SiO_2 surface to TEM grids (Quantifoil R2/2) by selective etching of the SiO_2 in 49% hydrofluoric acid. Images were acquired from different regions of the monolayer MoS_2 using a Nion UltraSTEM 100 aberration-corrected STEM in ADF-STEM mode with $E = 70$ kV. The beam convergence semi-angle was 30 mrad and the detector collection angle was in the range of 30-300 mrad, where a small detector inner angle was chosen to reduce the electron dose. The energy spread of the electron beam was 0.3 eV. To reduce the total electron dose, images were measured with a beam current of 15 pA and a dwell time of 84 μs per image, which correspond to a total electron dose 4.7×10^5 e$^-$/Å^2. The ADF-STEM images contain a mixture of Poisson and Gaussian noise and were denoised by the block-matching and 3D filtering (BM3D) algorithm[48], from which S vacancies were identified. It has been reported previously that a 80 keV electron beam induces S vacancies in MoS_2 with a rate of 3.45×10^8–3.36×10^9 electrons per S vacancy[3,21]. As we used a 70 keV electron beam, the vacancy formation rate in our experiment should be >3.45×10^8 electrons per S vacancy. From the total electron dose used in our experiment, we estimated the electron beam induced S vacancy density in our sample was <2×10^{20} cm^{-3}. Since we observed a S vacancy density of 3×10^{20} cm^{-3} in the MoS_2 sample, we concluded that the native S vacancy density was >1×10^{20} cm^{-3}, which is in agreement with that of exfoliated undoped MoS_2 samples[21].

DFT calculations. The calculations were performed using the Vienna ab initio simulation package (VASP) with the projector-augmented wave method[49,50]. The generalized gradient approximation of Perdew-Burke-Ernzerhof (GGA-PBE) was adopted for the exchange-correlation functionals[51]. The energy cutoff for the plane-wave expansion was set to 350 eV. Structure relaxation was stopped when the force on each atom was smaller than 0.01 eV/Å. The van der Waals interaction was included by using the correction scheme of Grimme[52].

For defect calculations in bulk MX2, we employed $5 \times 5 \times 1$ supercell, where a tilted c lattice vector was adopted, with $c = c_0 + 2a_0 + 2b_0$, where a_0, b_0, and c_0 are the primitive cell lattice vectors. As discussed in previous studies[1], this improves the convergence of total energies with respect to cell size. The k-point sampling is $2 \times 2 \times 2$. The defect charge-transition energy level $\varepsilon(q/q')$ corresponds to the Fermi energy E_F at which the formation energy for a defect α with different charge state q and q' equals with each other. It can be calculated by[53]:

$$\epsilon(q/q') = [E(\alpha, q) - E(\alpha, q') + (q - q')(E_{VB} + \Delta V)]/(q' - q).$$

Here E(α,q) is the total energy of the supercell containing the defect, and E_{VB} is the valence band maximum (VBM) energy of the host material. The potential alignment correction term ΔV is added to align the VBM energy in systems with different charged states. It is calculated by the energy shift of the 1s core-level energy of a specified atom (which is far away from the defect site) between the neutral defect and charged cases. For $Mo_{1-x}W_xS_2$ alloys, different S vacancy sites have different local environments. The number of surrounding Mo and W atoms varies, resulting in four types of V_S. We calculated the charge-transition levels for each type, and then carried out an average according to the concentration of different types to obtain the final charge-transition level.

Data availability
The data that support the plots in this paper are available from the corresponding author upon reasonable request.

References
1. Komsa, H.-P. & Krasheninnikov, A. V. Native defects in bulk and monolayer MoS 2 from first principles. *Phys. Rev. B* **91**, 125304 (2015).
2. Amani, M. et al. Near-unity photoluminescence quantum yield in MoS2. *Science* **350**, 1065–1068 (2015).
3. Qiu, H. et al. Hopping transport through defect-induced localized states in molybdenum disulphide. *Nat. Commun.* **4**, 1–6 (2013).
4. Pandey, M. et al. Defect-tolerant monolayer transition metal dichalcogenides. *Nano Lett.* **16**, 2234–2239 (2016).
5. Langer, J. M. & Heinrich, H. Deep-level impurities: a possible guide to prediction of band-edge discontinuities in semiconductor heterojunctions. *Phys. Rev. Lett.* **55**, 1414 (1985).
6. Hjalmarson, H. P., Vogl, P., Wolford, D. J. & Dow, J. D. Theory of substitutional deep traps in covalent semiconductors. *Phys. Rev. Lett.* **44**, 810 (1980).
7. Walukiewicz, W. Amphoteric native defects in semiconductors. *Appl. Phys. Lett.* **54**, 2094–2096 (1989).
8. Mooney, P. Deep donor levels (DX centers) in III-V semiconductors. *J. Appl. Phys.* **67**, R1–R26 (1990).
9. Barja, S. et al. Identifying substitutional oxygen as a prolific point defect in monolayer transition metal dichalcogenides. *Nat. Commun.* **10**, 1–8 (2019).
10. Cui, X. et al. Multi-terminal transport measurements of MoS 2 using a van der Waals heterostructure device platform. *Nat. Nanotechnol.* **10**, 534 (2015).
11. Tian, X. et al. Correlating the three-dimensional atomic defects and electronic properties of two-dimensional transition metal dichalcogenides. *Nat. Mater.* **19**, 867–873 (2020).
12. Amit, I. et al. Role of charge traps in the performance of atomically thin transistors. *Adv. Mater.* **29**, 1605598 (2017).
13. Yin, L. et al. Robust trap effect in transition metal dichalcogenides for advanced multifunctional devices. *Nat. Commun.* **10**, 1–8 (2019).
14. Ramasubramaniam, A. & Naveh, D. Mn-doped monolayer MoS 2: an atomically thin dilute magnetic semiconductor. *Phys. Rev. B* **87**, 195201 (2013).
15. Le, D., Rawal, T. B. & Rahman, T. S. Single-layer MoS2 with sulfur vacancies: structure and catalytic application. *J. Phys. Chem. C* **118**, 5346–5351 (2014).
16. Xie, J. et al. Defect-rich MoS2 ultrathin nanosheets with additional active edge sites for enhanced electrocatalytic hydrogen evolution. *Adv. Mater.* **25**, 5807–5813 (2013).
17. Vancsó, P. et al. The intrinsic defect structure of exfoliated MoS 2 single layers revealed by scanning tunneling microscopy. *Sci. Rep.* **6**, 29726 (2016).
18. Addou, R., Colombo, L. & Wallace, R. M. Surface defects on natural MoS2. *ACS Appl. Mater. interfaces* **7**, 11921–11929 (2015).
19. Liu, X., Balla, I., Bergeron, H. & Hersam, M. C. Point defects and grain boundaries in rotationally commensurate MoS2 on epitaxial graphene. *J. Phys. Chem. C* **120**, 20798–20805 (2016).
20. Jeong, T. Y. et al. Spectroscopic studies of atomic defects and bandgap renormalization in semiconducting monolayer transition metal dichalcogenides. *Nat. Commun.* **10**, 1–10 (2019).
21. Hong, J. et al. Exploring atomic defects in molybdenum disulphide monolayers. *Nat. Commun.* **6**, 1–8 (2015).
22. Lang, D. Deep-level transient spectroscopy: a new method to characterize traps in semiconductors. *J. Appl. Phys.* **45**, 3023–3032 (1974).
23. McCluskey, M. D. & Haller, E. E. *Dopants and defects in semiconductors.* (CRC press, 2018).
24. Liu, Y. et al. Approaching the Schottky–Mott limit in van der Waals metal–semiconductor junctions. *Nature* **557**, 696–700 (2018).
25. Borsuk, J. & Swanson, R. Current transient spectroscopy: a high-sensitivity DLTS system. *IEEE Trans. electron devices* **27**, 2217–2225 (1980).
26. Blood, P. & Orton, J. W. *The electrical characterization of semiconductors: majority carriers and electron states.* 2 (Academic press, London, 1992).
27. Almbladh, C.-O. & Rees, G. Statistical mechanics of electronic energy levels in semiconductors. *Solid State Commun.* **41**, 173–176 (1982).
28. Lagowski, J., Kaminska, M., Parsey, J. Jr., Gatos, H. & Lichtensteiger, M. Passivation of the dominant deep level (EL2) in GaAs by hydrogen. *Appl. Phys. Lett.* **41**, 1078–1080 (1982).
29. Vertiatchikh, A., Eastman, L., Schaff, W. & Prunty, T. Effect of surface passivation of AlGaN/GaN heterostructure field-effect transistor. *Electron. Lett.* **38**, 388–389 (2002).
30. Yu, P. Y. & Cardona, M. *Fundamentals of semiconductors: physics and materials properties.* (Springer, 1996).
31. Kang, J., Tongay, S., Zhou, J., Li, J. & Wu, J. Band offsets and heterostructures of two-dimensional semiconductors. *Appl. Phys. Lett.* **102**, 012111 (2013).
32. Ci, P. et al. Quantifying van der Waals interactions in layered transition metal dichalcogenides from pressure-enhanced valence band splitting. *Nano Lett.* **17**, 4982–4988 (2017).
33. Claeys, C. & Simoen, E. *Germanium-based technologies: from materials to devices.* (Elsevier, 2011).
34. Li, J. et al. Nature of Mg impurities in GaN. *Appl. Phys. Lett.* **69**, 1474–1476 (1996).
35. Lin, J., Dissanayake, A., Brown, G. & Jiang, H. Relaxation of persistent photoconductivity in Al 0.3 Ga 0.7 As. *Phys. Rev. B* **42**, 5855 (1990).
36. McCluskey, M. et al. Metastability of oxygen donors in AlGaN. *Phys. Rev. Lett.* **80**, 4008 (1998).
37. Chadi, D. & Chang, K.-J. Theory of the atomic and electronic structure of DX centers in GaAs and Al x Ga 1− x As alloys. *Phys. Rev. Lett.* **61**, 873 (1988).

38. Chand, N. et al. Comprehensive analysis of Si-doped Al x Ga 1− x As (x= 0 to 1): Theory and experiments. *Phys. Rev. B* **30**, 4481 (1984).
39. Chadi, D. & Chang, K.-J. Energetics of DX-center formation in GaAs and Al x Ga 1− x As alloys. *Phys. Rev. B* **39**, 10063 (1989).
40. Singh, A. & Singh, A. K. Origin of n-type conductivity of monolayer MoS 2. *Phys. Rev. B* **99**, 121201 (2019).
41. Fujisawa, T., Krištofik, J., Yoshino, J. & Kukimoto, H. Metastable behavior of the DX center in Si-doped GaAs. *Jpn. J. Appl. Phys.* **27**, L2373 (1988).
42. Tachikawa, M. et al. Observation of the persistent photoconductivity due to the DX center in GaAs under hydrostatic pressure. *Jpn. J. Appl. Phys.* **24**, L893 (1985).
43. Radisavljevic, B., Radenovic, A., Brivio, J., Giacometti, V. & Kis, A. Single-layer MoS 2 transistors. *Nat. Nanotechnol.* **6**, 147 (2011).
44. Chen, Y. et al. Tuning electronic structure of single layer MoS2 through defect and interface engineering. *ACS Nano* **12**, 2569–2579 (2018).
45. Liu, G.-B., Xiao, D., Yao, Y., Xu, X. & Yao, W. Electronic structures and theoretical modelling of two-dimensional group-VIB transition metal dichalcogenides. *Chem. Soc. Rev.* **44**, 2643–2663 (2015).
46. Guo, Y. & Robertson, J. Band engineering in transition metal dichalcogenides: Stacked versus lateral heterostructures. *Appl. Phys. Lett.* **108**, 233104 (2016).
47. Wang, G. et al. Spin-orbit engineering in transition metal dichalcogenide alloy monolayers. *Nat. Commun.* **6**, 1–7 (2015).
48. Dabov, K., Foi, A., Katkovnik, V. & Egiazarian, K. Image denoising by sparse 3-D transform-domain collaborative filtering. *IEEE Trans. Image Process* **16**, 2080–2095 (2007).
49. Kresse, G. & Furthmüller, J. Efficient iterative schemes for ab initio total-energy calculations using a plane-wave basis set. *Phys. Rev. B* **54**, 11169 (1996).
50. Blöchl, P. E. Projector augmented-wave method. *Phys. Rev. B* **50**, 17953 (1994).
51. Perdew, J. P., Burke, K. & Ernzerhof, M. Generalized gradient approximation made simple. *Phys. Rev. Lett.* **77**, 3865 (1996).
52. Grimme, S. Semiempirical GGA-type density functional constructed with a long-range dispersion correction. *J. Comput. Chem.* **27**, 1787–1799 (2006).
53. Wei, S.-H. Overcoming the doping bottleneck in semiconductors. *Comput. Mater. Sci.* **30**, 337–348 (2004).

Author contributions

P.C., O.D. and J.W. conceived this project. P.C. fabricated DLTS and PPC devices and completed the measurements, with the assistance from A.S., K.E., S.W., K.T., J.L., Y.C. and O.D. X.T. and J.M. contributed to atomic-resolution STEM imaging. S.T. grew the bulk MoS2, WS2 and alloys. J.K. performed DFT calculations. P.C., J.K., W.W. and J.W. analyzed the results. All authors discussed and contributed to the preparation of the manuscript.

Competing interests

The authors declare no competing interests.

Additional information

Supplementary information is available for this paper at https://doi.org/10.1038/s41467-020-19247-1.

Correspondence and requests for materials should be addressed to J.W.

Peer review information *Nature Communications* thanks Abdelmadjid Mesli and the other, anonymous reviewer(s) for their contribution to the peer review of this work. Peer review reports are available.

Reprints and permission information is available at http://www.nature.com/reprints

Publisher's note Springer Nature remains neutral with regard to jurisdictional claims in published maps and institutional affiliations.